

DERIVATION OF DIGITAL TERRAIN MODELS BY MEANS OF MULTI-IMAGE SHAPE-FROM-SHADING: RESULTS USING CLEMENTINE IMAGES

Volker Lohse , Christian Heipke

University of Hannover, Institute of Photogrammetry and GeoInformation, Nienburger Straße 1,
30167 Hannover, Germany - (lohse, heipke)@ipi.uni-hannover.de

KEY WORDS: Digital terrain models, planetary surfaces, multi-image shape-from-shading, Clementine

ABSTRACT:

This paper describes a method for the generation of high-resolution digital terrain models (DTMs) from planetary surfaces using optical images. In many cases, the solution of this task using conventional digital image matching is a problem: The matching methods need at least a stereo pair of images with sufficient texture. Often though, during space missions only few stereo images are acquired and, furthermore, many planetary surfaces only show little grey value variations. The suggested method, here termed "multi-image shape-from-shading" (MI-SFS), is able to generate a planetary DTM with an arbitrary number of images of low texture. Therefore, MI-SFS is a suitable method in areas, in which image matching fails to yield a DTM. The paper contains a short review of the theory of MI-SFS, followed by a description and discussion of the first results, which were obtained with images from NASA's lunar mission Clementine.

1. INTRODUCTION

In planetary science digital terrain models (DTMs) are an important data set for many applications such as the description of local and regional topographic features, slopes and thus possible flow direction of liquid material and isostatic considerations to name only a few. On Earth, such DTMs can normally be derived via conventional photogrammetry inclusive digital image matching. However, planetary missions in general are not topographic missions, and thus often there are only a few or no stereoscopic images available. Additionally, some planetary stereo pairs have a disadvantageous camera configuration (e.g. a poor base-to-height ratio) and in many cases planetary images comprise poor image texture, which is an obstacle to automatic matching methods. Therefore, in many areas no complete high-resolution DTM of planetary bodies can be made available by means of conventional photogrammetric methods. Thus, it is necessary to close these gaps in the DTM with other reconstruction methods, which are able to work with a single image and/or with images including low texture, such as "multi-image shape-from-shading" (MI-SFS).

MI-SFS has been developed by our group over the last decade. A detailed description including results with simulated and aerial images from a desert area on Earth are given in (Heipke, 1992; Heipke, Piechullek, 1994; Piechullek, 2000). In this paper we present for the first time results using planetary images, more precisely images from NASA's lunar mission Clementine.

2. THEORY OF MI-SFS

For solving the DTM reconstruction problem by "shape-from-shading" (SFS), the image formation process has to be modelled and inverted with respect to the parameters describing the object space (Horn, Brooks, 1989). Like other SFS methods, MI-SFS is based on the fact that surface patches, having different inclination relative to the light source, are imaged with

different brightness, and makes use of these variations in the recorded grey values to infer the underlying surface.

In contrast to classical SFS methods, MI-SFS can deal with an arbitrary number of images, is based on perspective transformation between image and object space and relates directly the grey values to the heights of a DTM and the parameters of a radiometric model, which describes the surface reflectance behaviour. The DTM heights as well as the parameters of the radiometric model are estimated from the image grey values in a least-squares adjustment.

For MI-SFS it is assumed that the albedo is constant across the area under consideration. If the albedo is not constant the reconstruction will produce local systematic errors, because MI-SFS does not differ between albedo- and topographical variations as reasons for grey value variation in image space, and thus albedo variations will be interpreted as variations in heights. A solution for areas with varying albedo is given by pre-processing the images in a suitable way, which is, however, outside the scope of this paper.

An elementary reflectance model for describing the bi-directional reflectance (BDR) from a surface is the Lambert law. Specific descriptions and equations of the Lambert law and the corresponding reflectance models can be found in (Horn, 1986; Kraus, Schneider, 1988; Horn, Brooks, 1989; Horn, 1990; Hapke, 1993; Zhang et al., 1994). The Lambert model is based on the assumption that the brightness of a surface depends only on the incidence angle i between the direction of illumination \vec{s} and the surface normal \vec{n} (see figure 1). This means that the surface looks equally bright from every viewing direction. The Lambert model characterizes the reflectance from bright surfaces very well.

In order to extend the assumption that light reflection occurs at the boundary surface between two media only, the Lommel-Seeliger law was derived by Seeliger 1887 (Horn, Brooks, 1989; Hapke, 1993; Rebhan, 1993). In this model, light scattering is assumed to take place at the individual particles within a layer of infinite thickness below the apparent surface;

the irradiance observed at a sensor comes from light scattered by all particles in the medium lying within the field of view of the sensor. Therefore, the Lommel-Seeliger law does not only contain the incidence angle i but also the emittance angle e between surface normal \vec{n} and viewing direction \vec{v} (see again figure 1). The significant increase in brightness for large emittance angles e is due to the fact that with increasing e the area of the imaged surface also increases, and thus a greater part of the surface layer contributes to the brightness observed in the sensor. In contrast to the Lambert law, the Lommel-Seeliger law describes dark surfaces better.

Using the Lommel-Seeliger reflectance a model grey value $G(x',y')$ in image space can be formulated based on the well-known camera equation (e.g. Horn, 1986):

$$G(x', y') = k \frac{\pi}{4} \cos^a(\gamma) \left(\frac{d}{f}\right)^2 E_s \rho(X, Y) \frac{2 \cos(i)}{\cos(i) + \cos(e)} \quad (1)$$

$$\text{with} \quad \cos(e) = \frac{\vec{n} \cdot \vec{v}}{|\vec{n}| |\vec{v}|} \quad \text{and} \quad \cos(i) = \frac{\vec{n} \cdot \vec{s}}{|\vec{n}| |\vec{s}|}$$

where $G(x',y')$ = model grey value at image point P'
 x',y' = image coordinates of point P' (projection of P into image space)
 k = rescaling constant for transformation of image irradiance into model grey value $G(x',y')$
 a = exponent of light fall-off
 γ = angle between optical axis and the ray through P and P'
 d = diameter of optical lens
 f = focal length of optical lens
 E_s = scene irradiance
 $\rho(X,Y)$ = albedo of the object surface
 \vec{n} = normal vector of the object surface at P(X,Y,Z)
 \vec{s} = unit vector in illumination direction at P(X,Y,Z)
 \vec{v} = unit vector in viewing direction at P(X,Y,Z)

Next, the scene irradiance E_s , the sensor parameters (a , d , f , k and γ) and the albedo ρ are assumed to be constant and are combined into a so called reflectance coefficient A_R :

$$A_R = k \frac{\pi}{4} \cos^a(\gamma) \left(\frac{d}{f}\right)^2 E_s \rho(X, Y) \quad (2)$$

Thus, the model grey value G depends on the reflectance coefficient A_R and on the illumination direction \vec{s} , the viewing direction \vec{v} and the local surface normal \vec{n} :

$$G(x', y') = f(A_R, \vec{s}, \vec{v}, \vec{n}) = A_R \frac{2 \cos(i)}{\cos(i) + \cos(e)} \quad (3)$$

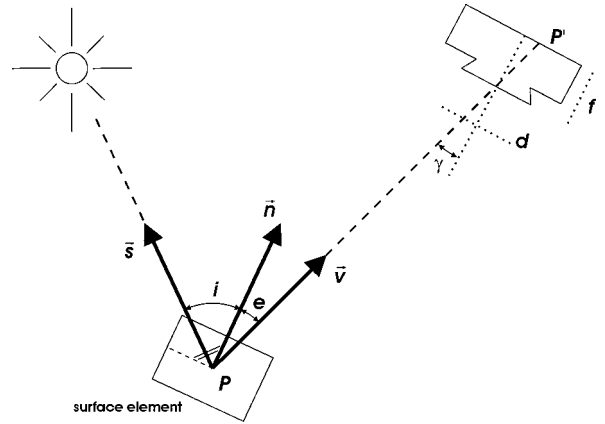


Figure 1. Camera parameters and the relationship between \vec{s} , \vec{n} , \vec{v}

In this approach the light source is assumed as a distant point light source with known position. The atmospheric influences are considered to be constant, and thus part of A_R . In addition, the sensor parameters are assumed to be known from radiometric and geometric calibrations.

In order to appropriately describe the object surface, a geometrical and a radiometrical surface model are introduced. The geometrical model consists of a DTM grid. The grid is defined in the XY-plane of the object space with grid nodes X_k , Y_l and corresponding grid heights $Z_{k,l}$. The mesh size of the grids depends on the roughness of the terrain. A height Z at an arbitrary point is interpolated from the neighbouring grid heights, e.g. by bilinear interpolation. At each point of the object surface, the surface normal \vec{n} and thus the angles i and e become a function of the neighbouring $Z_{k,l}$.

For relating the geometric surface model to the behaviour of reflectance of the surface, a radiometric surface model is introduced. Object surface elements of constant size are defined within each DTM grid mesh. The size is chosen approximately equal to the pixel size multiplied by the average image scale factor. Each object surface element is assigned the same reflectance coefficient A_R .

If we assume the direction of illumination \vec{s} and the parameters of the orientation of all images and thus also \vec{v} to be known, the only unknown parameters for computing the model grey value $G(x',y')$ of equation (3) are the parameters of the object surface model, the DTM heights $Z_{k,l}$ and the reflectance coefficient A_R . For each image j the considered object surface element can be projected into image space using the collinearity equations and at that position $P'(x',y')$ the image grey value $g_j(x',y')$ can be resampled from the original grey values. The g_j are considered as observations in a least-squares adjustment for the estimation of the unknowns. The corresponding observation equations read:

$$v_j(x', y') = G(\hat{Z}_{k,l}, \hat{A}_R) - g_j(x'(\hat{Z}_{k,l}), y'(\hat{Z}_{k,l})) \quad (4)$$

where $v_j(x',y')$ = residuals of observation of observed grey value in image j

$\hat{Z}_{k,l}$ = DTM-heights (k - column; l - row), unknown

\hat{A}_R = reflectance coefficient, unknown

G = model grey value

g_j = observed grey value in image j

and after substituting equation (3) into equation (4) we obtain:

$$v_j(x', y') = \hat{A}_R \frac{2 \cos(i(\hat{Z}_{k,l}))}{\cos(i(\hat{Z}_{k,l})) + \cos(e_j(\hat{Z}_{k,l}))} - g_j(x'(\hat{Z}_{k,l}), y'(\hat{Z}_{k,l})) \quad (5)$$

Equation (5) is non-linear with respect to $\hat{Z}_{k,l}$, and therefore initial values have to be available for the unknown object space parameters $\hat{Z}_{k,l}$ and \hat{A}_R for carrying out the least-squares adjustment.

3. MI-SFS INVESTIGATIONS USING REAL DIGITAL PLANETARY DATA

The developed MI-SFS method has been tested for the first time with real digital planetary images. Here, we report on the results using one image only. Experiments with multiple images are still under way.

3.1 Input information

For the investigations we need the following input data and additional information:

- one or more digital planetary images of the same area with different viewing directions
- interior and exterior orientation of the images
- position of the sun during image acquisition
- initial values for the unknown DTM-heights and the unknown reflectance coefficient

We decided to use images from the lunar mission Clementine to demonstrate our method. Suitable overlapping images with different viewing directions to the same region and the required information was kindly provided by the Deutsche Zentrum für Luft- und Raumfahrt (DLR) in Berlin.

The Clementine mission was a joint project between the Ballistic Missile Defense Organization (BMDO) and the National Aeronautics and Space Administration (NASA). The aim of Clementine was the scientific observation of the moon. The mission ran from January to June 1994. A detailed description of the Clementine mission is published in (Nozette et al., 1994).

The main instruments of Clementine consisted of four cameras and a laser-ranging system. Over the course of 71 days, Clementine systematically mapped the 38 million square kilometres of the moon at eleven different wavelengths.

For our investigations we selected images from the Ultraviolet/Visible (UVVIS) digital frame camera, because these images best conform to our requirements. The UVVIS is a medium resolution camera with CCD-technology and operates in the region of the spectrum from 0.3 μm to 1.0 μm . The camera is arranged with a six-position spectral filter wheel. In table 1 some technical information of the UVVIS camera is given. In our experiments we used images from the UVVIS filter C (0.9 μm).

Specification	UVVIS
Field of view (FOV)	4.2° x 5.6°
Focal length	90 mm
Image array (height x width)	288 pixel x 384 pixel
Pixel size	23 μm x 23 μm
Radiometric resolution	8 Bit

Table 1. Technical data of the UVVIS camera

To derive a DTM with MI-SFS, we chose two images (figure 2), which were taken by the Clementine UVVIS camera from different orbits. The selected area of the moon is part of the "Northern Mare Orientale Basin" and lies between 16.3° and 14.3° South and 87.3° and 90.9° West. The image parameters are listed in table 2. The image No. 1 is a nadir image from the selected area acquired during orbit 333. The image No. 2 was recorded during orbit 338, when the camera was tilted sideways over the same region.

The two images have a nominal radiometric resolution of 8 Bit. Some artefacts which are probably due to image compression are visible, mainly as horizontal stripes in the images. Before the delivered images could be used by MI-SFS, they had to be radiometrically corrected. To perform the radiometric correction to the images we used the ISIS program UVVISCAL (USGS, 2003). UVVISCAL performs dark subtraction, readout correction, non-linearity and flat field correction. This program writes the output image values as radiance values [unity: $\text{W} \cdot \text{sr}^{-1} \cdot \text{m}^{-2}$].

Image No.		1	2
Orbit		333	338
Start time		1994-04-30 09:13	1994-05-01 10:24
Description		nadir	oblique
exterior orientation	X ₀ [km]	-14.0	-532.0
	Y ₀ [km]	-5.3	-26.2
	Z ₀ [km]	553.8	489.4
	ϕ [grad]	-1.6	-52.0
	ω [grad]	0.3	2.5
	κ [grad]	199.8	-196.9
Camera-to-object distance [km]		553.1	718.7
Spacecraft altitude [km]		552.9	549.9
Image scale		1 : 6146000	1 : 7986000
Ground resolution [m]	column	1 pixel \approx 141	1 pixel \approx 270
	row	1 pixel \approx 141	1 pixel \approx 183
Direction of illumination	horizontal [grad]	25.2	39.9
	vertical [grad]	59.3	71.2

Table 2. Image parameters

The geometric resolution of one pixel in image No. 1 is about 140 metres in row and column direction. The oblique-image (image No. 2) has a resolution of about 180 metres in row and 270 metres in column direction. For the computation of the illumination vectors the sun position at the time of image acquisition was used (see table 2). In figure 3 a graphical overview of the configuration of the images and the situation of the illumination directions of each image is depicted.

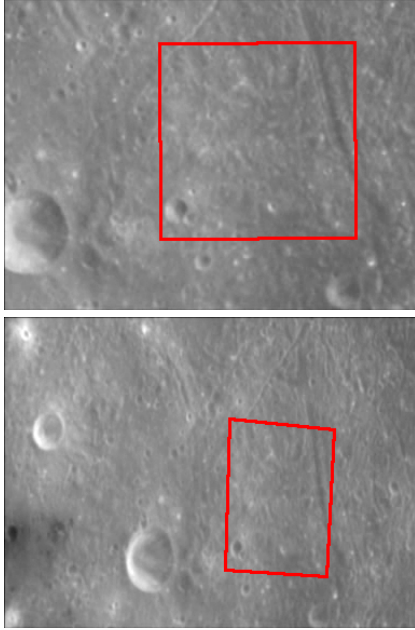


Figure 2. Selected area in northwards direction: nadir-image No. 1 (above), oblique-image No. 2 (below)

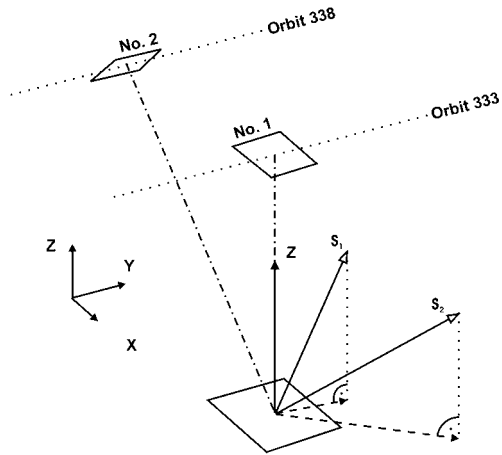


Figure 3. Camera configuration and situation of illumination direction at the time of recordings

The two images were recorded with a time difference of about 25 hours. We assume that during this period of time no changes happened in the observed area.

In the overlapping part of the two images an area with the size of about 25.5 km times 25.5 km was chosen. The altitude difference in this region is about 1.3 kilometres. This selected area is marked in red in the two images (see figure 2).

The surface in the selected area was divided into 34 x 34 DTM grids with a mesh size of 750 metres. Thus, there were 1225 DTM-heights. Each grid mesh consisted of 5 x 5 object surface elements. This means that each object surface element had a size of 150 x 150 m², which is approximately the same as one pixel in the images.

3.2 Initial DTMs, reference DTM and further specifications

Our first aim was to demonstrate that the MI-SFS method is independent of the chosen initial values for the unknowns, a requirement which is of course essential for any iterative method. For this purpose we have chosen three different initial

DTMs. The first one was an undulated DTM. This DTM was generated by means of a digital photogrammetric workstation. The DTM was manually measured three times by two different operators. The average values of the three measurements constitute the initial DTM (DTM_A, see figure 4). The average value of the standard deviations of DTM_A is about 80 metres, which is approximately half a pixel. The initial DTM_B is a DTM which differ from DTM_A by a scale factor m of 0.5 (see equation 6). The third initial DTM is a horizontal plane (DTM_C), this means m is set to 0. Thus, all heights of DTM_C reach the value of -3 metres, which is the average height of DTM_A.

$$Z_{Xi} = \bar{Z}_A + m(Z_{Ai} - \bar{Z}_A) \quad (6)$$

where Z_{Ai} = DTM-height number i of the reference DTM_A
 \bar{Z}_A = average value of the reference DTM_A
 Z_{Xi} = DTM-height number i of the destination DTM_X
 m = scale factor

DTM_A serves two purposes: it was used as one of the three initial DTMs, and it is also used as reference DTM. This means that the results of MI-SFS should be very close to DTM_A, irrespective of whether DTM_A, DTM_B or DTM_C was used as initial DTM.

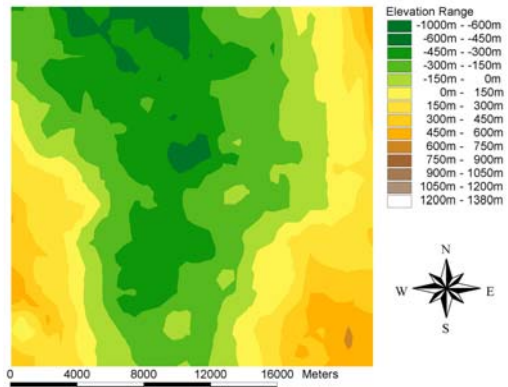
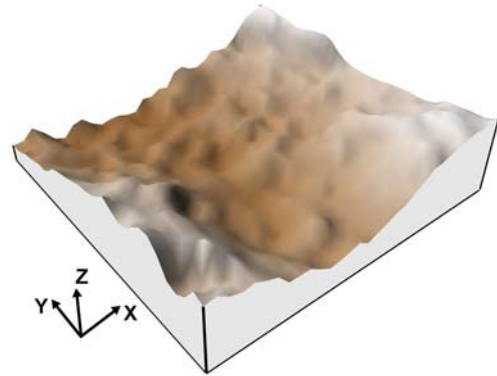


Figure 4. Reference DTM, also used as initial DTM_A: exaggeration of height-factor = 5 (above), coloured height values (below)

The experiments were made with the assumption that the selected surface has the properties of Lommel-Seeliger-reflectance. For the whole selected surface it was assumed that

the reflectance coefficient A_R was constant. The initial value for A_R was set to 5, which was approximately the average radiance value of the calibrated images. The criterion for stopping the iterative computations was that the correction for each unknown height was below 50 metres (one third of a pixel).

As mentioned above, the investigations discussed here were carried out with one image only. For this analysis we have chosen image No. 2, because a nadir image by itself cannot be used within MI-SFS since the grey value changes with respect to height changes are generally too small to allow for a numerically stable solution (see Piechullek, 2000 for details). Analyses with two and more images are in process, as well as analyses with the assumption of Lambertian-reflectance.

3.3 Results

The resulting DTMs using image No. 2 and the three different initial DTMs are shown in figure 5. The comparisons of the 3D-views shows that the results are more or less identical.

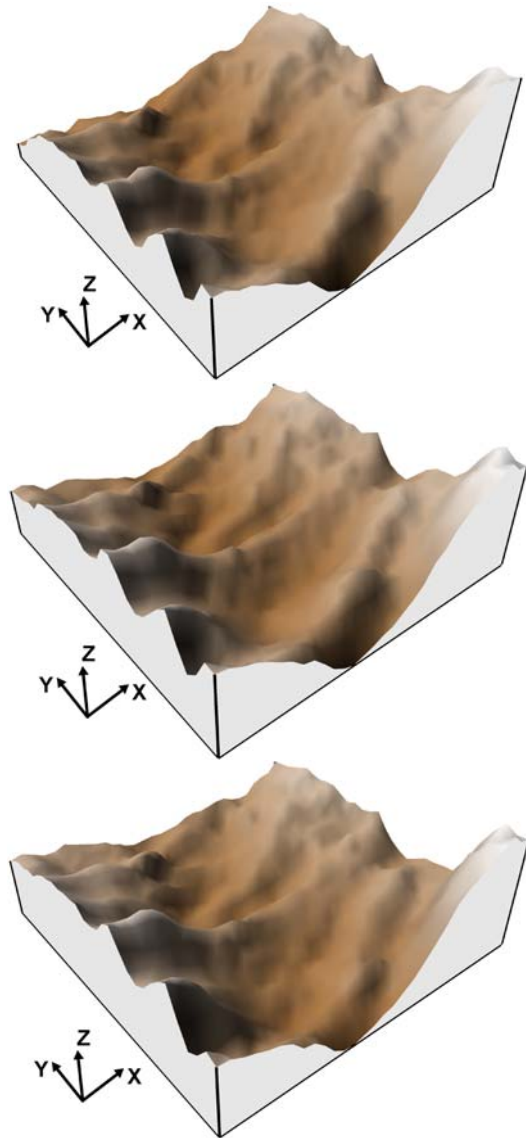


Figure 5. Results with image No. 2 (heights are exaggerated by the factor 5): initial DTM_A (above), initial DTM_B (middle) and initial DTM_C (below)

The numerical results of the comparisons for the three MI-SFS results, each with an different initial DTM, are shown in table 3. Comparison No. 1 demonstrate that since the average height difference $\bar{\Delta Z}$ and the standard deviation $s_{\Delta Z}$ are rather small the radius of convergence of our MI-SFS method is at least 650 metres (the height difference between initial DTM_A and initial DTM_B) which is approximately 5 pixels. An exception can be seen at the top left and the bottom right corner with larger differences between the two results (see figure 6). In these regions the differences amount to 460 metres. At present we are investigating the cause of these findings.

In contrast to the result of comparison 1, those of comparison 2 show, that DTM_C probably lies outside the radius of convergence, possibly due to image noise and/or the mentioned compression artefacts. We are currently investigating the possibility to extend the radius of convergence by reducing these two causes via low-pass filtering.

Comparison	Image No.	1. Initial DTM	2. Initial DTM	$\bar{\Delta Z}$ [m]	$s_{\Delta Z}$ [m]
1	2	DTM _A	DTM _B	13.1	47.8
2	2	DTM _A	DTM _C	55.7	97.8

Table 3. Comparison between the results with initial DTM_A, initial DTM_B and initial DTM_C

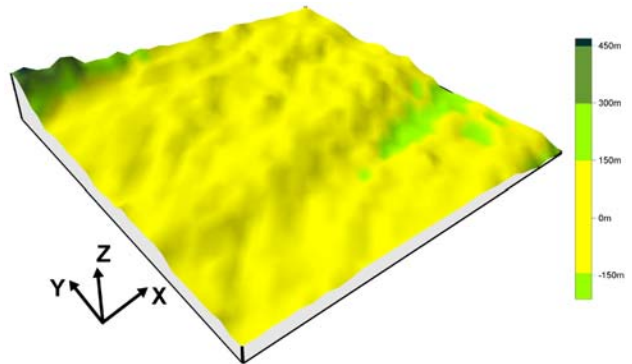


Figure 6. Differences between the results with initial DTM_A and initial DTM_B (factor of height-exaggeration = 5)

Our second goal was then to check the geometric accuracy of MI-SFS. We did so by comparing the obtained results to the manually acquired reference DTM (the DTM_A introduced above). Table 4 shows the numerical results of the analyses. For the comparison the following parameters are computed: the minimum, maximum and the average height difference (ΔZ_{\min} , ΔZ_{\max} and $\bar{\Delta Z}$) and the standard deviation of the heights differences ($s_{\Delta Z}$). Additionally, the reflectance coefficient A_R is given.

Image No.	Initial DTM	ΔZ_{\min} [m]	ΔZ_{\max} [m]	$\bar{\Delta Z}$ [m]	$s_{\Delta Z}$ [m]	A_R [W*sr ⁻¹ *m ²]
2	DTM _A	-660.2	407.1	-18.5	163.5	3.49
2	DTM _B	-600.1	462.8	-5.5	198.2	3.47
2	DTM _C	-636.7	701.2	37.1	263.3	3.46

Table 4. Comparison between the reference DTM and the MI-SFS results assuming Lommel-Seeliger reflectance

The results with initial DTM_A and initial DTM_B show a very small shift $\bar{\Delta Z}$ and a standard deviation $s_{\Delta Z}$ of approximately one pixel (see also figure 7). Taking the accuracy of the reference DTM into account (half a pixel, see above) these results can be considered satisfactory, indicating an accuracy of our method of one pixel (and possibly better). As was to be expected, the result with the flat initial DTM_C is worse than with the undulated DTMs. As mentioned above, it seems that the initial DTM_C is outside of the radius of convergence.

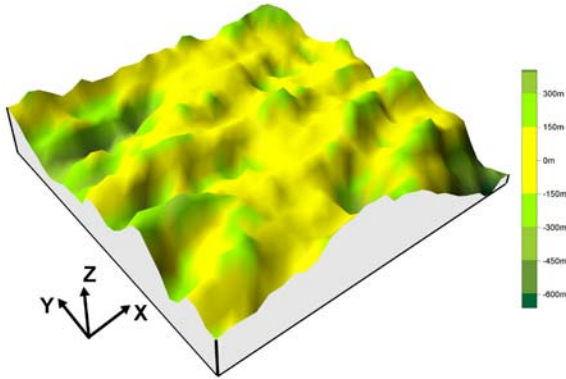


Figure 7. Differences between reference DTM and result with initial DTM_A (factor of height-exaggeration = 5)

The selected area is presented in figure 8. The illumination direction comes from the north-east (see also table 2). With the 3D-views (see figure 5) and the image of the selected area, it is possible to compare rough structures. The Eastern part of the image (figure 8) is darker than the rest, which corresponds to the fact that the DTM is tilted away from the light source. In the Western part of the image, the grey values are generally brighter, and correspondingly the DTM is tilted towards the light source. In the top-right corner of the selected area there is a valley running from east to north. This valley can not be seen in the DTMs. Also other distinct features that are visible in the image, like craters, do not show up in the DTMs, probably because the mesh size of about 750 metres does not allow representing these features in the reconstructed DTMs.

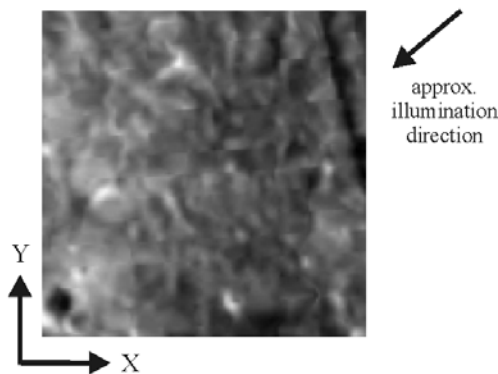


Figure 8. Originally selected area

The comparison between the residuals of the grey values and the selected area (see figure 9) shows that in the residuals distinct features like valleys and craters (three examples are marked) can be seen. The previously discussed qualitative analysis of the DTM and the structures in the residuals are an indication that the grid size of 750 metres employed in the described tests is too large.

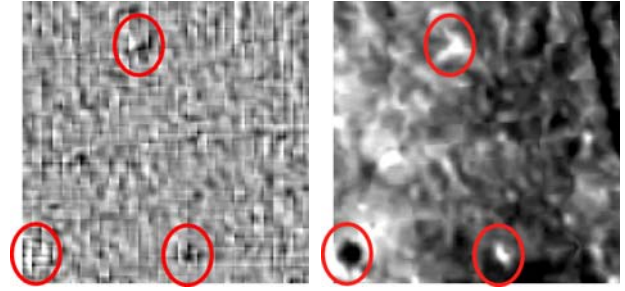


Figure 9. Residuals of grey values with image No. 2 and DTM_A (left), originally selected area (right)

Therefore, the selected area was divided into smaller DTM grid meshes.

First investigations were made with a mesh size of 3 times 3 object surface elements (450 metres instead of 750 metres). The selected area for this analysis lies in the bottom left area of the first used region above and is called area No. 2 in the following (the area with the larger mesh sizes is called area No. 1).

The statistical values of the analysis from area No. 2 have not changed significantly in comparison with the results from area No. 1. However, the visible structures in the residuals have decreased (figure 10 left).

These results indicate that using a geometrical object model with a smaller mesh size is a promising way to enhance the quality of our results. The refinement of the geometrical object surface model to a model with a mesh size of only one times one object surface elements is a component of our future work.

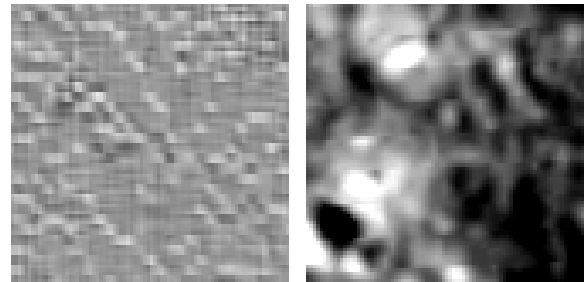


Figure 10. Residuals of grey values with image No.2 and DTM_A of area 2 (left), originally selected area (right)

4. CONCLUSIONS

The represented work on MI-SFS shows for the first time that the derivation of a high-resolution DTM of real digital planetary images by means of MI-SFS is feasible.

In detail we obtained the following results using imagery from the lunar mission Clementine:

- the method has a radius of convergence of at least five pixel
- the method has a geometric accuracy of approximately one pixel and possibly better
- very high-resolution variations of the topographic object surface can be captured

In future we will extend our investigations to simultaneously process two and more images within MI-SFS. We will also try to extend the radius of convergence by proper image pre-processing and to increase the geometric accuracy by introducing more sophisticated object surface models (one

times one pixel DTMs with appropriate smoothness constraints, breakline and occlusion detection modules).

In addition, the next important step is the combination of image matching with MI-SFS to a combined method. The rationale for this integration of the two methods is that when applied in isolation both methods may fail to achieve the desired results with planetary images. However, they have complimentary pre-conditions in terms of the image texture, and therefore, an integration of the two methods is believed to yield better results. A pre-requisite for such a combination is a separation of the area under consideration into parts with constant albedo (to be treated with MI-SFS) and parts with variable albedo (to be processed with image matching). This task remains a challenge of the whole approach which we will try to tackle using texture analysis.

REFERENCES

Hapke, B., 1993. *Theory of Reflectance and Emittance Spectroscopy, Topics in remote sensing Vol. 3*, New York, Cambridge University Press.

Heipke, C., 1992. Integration of digital image matching and multi image shape from shading. *International Archives of Photogrammetry and Remote Sensing*, Washington, Vol. XXIX, Part B3, pp. 832-841.

Heipke, C., Piechullek, C., 1994. Towards surface reconstruction using multi image shape from shading. *International Archives of Photogrammetry and Remote Sensing*, Vol. XXX, Part 3/1, pp. 361-369.

Horn, B. K. P., 1986. *Robot Vision*. The MIT Press.

Horn, B. K. P., 1990. Height and Gradient from Shading. *International Journal of Computer Vision* 5(1), pp. 37-75.

Horn, B. K. P., Brooks, M. J., 1989. *Shape from Shading*. The MIT Press.

Kraus, K., Schneider, W., 1988. *Fernerkundung Band 1: Physikalische Grundlagen und Aufnahmetechniken*. Bonn, Dümmler.

Nozette, P. et al., 1994. The Clementine mission of the moon. *Science*, Vol. 266, pp. 1835-1839.

Piechullek, C., 2000. Oberflächenrekonstruktion mit Hilfe von einer Mehrbild-Shape-from-Shading-Methode. *Deutsche Geodätische Kommission, Reihe C, Heft 518*.

Rebhan, H., 1993. Richtungsabhängige Reflexionseigenschaften der lunaren Oberfläche. *Dissertation, Deutsche Forschungsanstalt für Luft- und Raumfahrt, Oberpfaffenhofen, DLR-Forschungsbericht 93-28*.

USGS, 2003. ISIS 2.1: Integrated Software for Imagers and Spectrometers. <http://www.flag.wr.usgs.gov/ISIS> (accessed 16 Jul. 2003).

Zhang, R., Tsai, P.-S., Cryer, J. E., Shah, M., 1994. Analysis of Shape from Shading Techniques. *Proceedings of the IEEE Computer Society Conference on Computer Vision and Pattern Recognition*, Seattle, Washington, pp. 377-384.

5. ACKNOWLEDGEMENT

This work was developed within the priority program "Mars and the terrestrial planets" financed by the Deutsche Forschungsgemeinschaft (DFG) under the project number HE 1820/10.

Thanks to the DLR and especially to Marita Wählisch for providing the Clementine data and many interesting discussions. Furthermore, thanks to the employees of the ISIS Support Center at the United States Geological Survey (USGS) for their aid in the radiometric calibration of the Clementine images.